Crack monitoring in historical masonry with distributed strain and acoustic emission sensing techniques.

[1]Els Verstrynge, [1]Kristof De Wilder, [1]Anastasios Drougkas, [2]Eli Voet, [1]Koen Van Balen, [3]Martine Wevers

[1]Building Materials and Building Technology Division, Civil Engineering Department, KU Leuven, Belgium
[2]Com&Sens, Ghent University, Belgium
[3]Department of Materials Engineering, KU Leuven, Belgium.

Corresponding author: els.verstrynge@kuleuven.be

Abstract

The analysis of crack patterns and crack growth is one of the most important steps in the assessment of structural damage in historical masonry. In a search for integrated and accurate monitoring techniques for crack measurements in masonry, several novel techniques based on distributed strain monitoring and acoustic emission (AE) sensing have been investigated in an experimental test campaign. Aim of the test program was to develop integration procedures for the strain and AE sensors, analyse their use for crack monitoring specifically in historical masonry and assess their robustness and efficiency with respect to the experimentally observed crack pattern. The applied techniques were integrated optical fibres with distributed fibre Bragg grating sensors (FBGs), stereo-vision digital image correlation (DIC) without the use of a speckle pattern, optical fibre sensors for acoustic emission sensing (AE-FOS), piezo-electric transducers for acoustic emission sensing (AE-PZT) and LVDTs. While the latter two were applied as reference techniques, the former three were under investigation as novel application. This paper discusses the efficiency of the monitoring techniques with respect to their use in masonry, explains the developed integration procedures, and relates the obtained data sets with the deformations and crack pattern obtained in a full-scale masonry wall test. Additionally, the effects of temperature fluctuations are investigated. The configurations that were developed proved effective for crack monitoring in historical masonry. The highest sensitivity and robustness was observed for the integrated optical fibres with FBGs.

This is an open access preprint version of the paper that was published as:

Verstrynge, E., De Wilder, K., Drougkas, A., Voet, E., Van Balen, K., Wevers, M. (2018). Crack monitoring in historical masonry with distributed strain and acoustic emission sensing techniques. Construction and Building Materials, 162, 898-907. doi: 10.1016/j.conbuildmat.2018.01.103

1 INTRODUCTION

Structural cracking in unreinforced, historical masonry can be caused by differential settlements, creep and fatigue, vibrations and earthquakes, impact, temperature- and load-induced stresses. Depending on the cause and severity of the damage, cracking in masonry might lead to loss of cohesion in load-bearing walls, reduction of structural capacity and even collapse in case of unstable crack growth [1], loss of static equilibrium or additional earthquake loading. As the crack patterns provide vital information on the cause and severity of the damage, mapping and monitoring of the structural cracks is one of the most important steps in the assessment of damage [2]. In severe cases, crack widths are to be monitored to assess the damage progress and ascertain the structural integrity of the monument.

Monitoring techniques for detection of structural damage in existing structures can be divided in local and global techniques. At the scale of materials and structural components, local monitoring methods, such as crack measurements, mostly focus on individual cracks and displacements, and might therefore not provide enough information to address the overall structural integrity. At the structural scale, a well-known global method is the vibration-based method, in which changes in modal characteristics are monitored to detect the initiation or increase of damage [3, 4]. For historical masonry structures, the type of information to be gathered and the data processing to be done in order to optimise vibration-based damage analysis is not always straightforward. The efficient application of such global methods for detection, localization and quantification of “local” damage in existing structures remains a major challenge for the research community, especially under ambient vibrations and for heritage structures. Distributed sensor networks are applied for upscaling local and global methods. At the scale of a building, local strain sensors and accelerometers can be combined in a system with other devices, such as temperature and humidity sensors, to enable linking of the output data. As such, a multi-scale sensor network allows a more comprehensive understanding of the structural behaviour and damage progress, and results can be used for calibration or evaluation of numerical models [5, 6].

At regional scale, global monitoring techniques can be coupled in a network to allow monitoring of several structures at once and relate their behaviour and observed damage with detected ground motions, such as earthquakes or differential settlements. For monitoring of differential settlements, remote sensing techniques such as terrestrial laser scanning at the scale of building blocks, aerial laser scanning at city scale or Persistent Scatterer Interferometric Synthetic Aperture Radar (PS-InSAR) at regional scale can be applied [7-9].

This paper focusses on the monitoring of settlement-induced cracking at the scale of historical masonry walls, to obtain reliable monitoring data at the scale of a structural component that can be coupled to (settlement) data obtained at the scale of building blocks. Traditional crack monitoring devices, such as tell tales, crack width meters, LVDTs and DEMEC measurements have certain drawbacks with respect to upscaling; They can only locally detect 1D displacements, they often need to be reachable for read-outs, it is laborious to integrate them in a distributed sensor network and they cannot be integrated within the structure, thus remain visible. However, these techniques also have the advantage of long-term reliability and limited data drift.

In this work, distributed strain and acoustic wave sensing are investigated for crack monitoring in masonry. Optical fibre sensor systems are applied, which can combine the accuracy of local sensors with the advantages of distributed sensor networks. In total, five different techniques have been applied on a full-scale masonry wall during an experimental three-point-bending test. In addition, temperature data and load-displacement data were also recorded.

The applied techniques are:

- Optical fibres with distributed Fibre Bragg Grating sensors (FBG)[10];
- Digital Image Correlation (DIC), without the use of a speckle pattern;
- Optical Fibre Sensors for Acoustic Emission sensing (AE-FOS) [11];
- Piezo-electric transducers for Acoustic Emission sensing (AE-PZT) [12];
- Linear Variable Differential Transducers for displacement measurements (LVDTs).

While the latter two were applied as reference techniques, the former three were under investigation as novel applications. A prerequisite for the selection of the applied techniques was their ability to be integrated within the masonry or to be applied as a non-contact technique. The optical fibre sensors were integrated within the masonry's bed joint and digital image correlation was applied without the use of a speckle pattern. As cracks were expected in the mortar joints, strain-based techniques needed to include or bridge these weak areas in the structure. In comparing the results of the different monitoring techniques, specific attention was focused on accuracy, temperature influences and possibilities for on-site application. The investigated systems can be seen as distributed sensor networks of local sensors.

Firstly, the novel crack monitoring techniques and developed installation procedures are discussed. Secondly, the experimental test setup and loading scheme are briefly introduced. Hereafter, the results of the FBG, DIC and AE measurements are presented and compared with the results of the reference techniques. A discussion on the robustness, accuracy and temperature influences concludes this paper.

2 MONITORING TECHNIQUES AND INSTALLATION PROCEDURES

2.1 Optical fibre with distributed FBGs

Strain monitoring with optical fibres engraved with Bragg gratings relies on the analysis of the wavelength spectrum that is reflected by the Bragg gratings. If a change in length of the optical fibre occurs, a shift in the reflected wavelength is induced, where a positive shift in wavelength is related to elongation of the fibre [10, 13]. The length change may be caused by a mechanical strain or by thermal expansion.

In the reported lab experiment, an optical fibre type SMW-01 based on Draw Tower Gratings technology has been applied. The optical fibre with a primary ORMOCER coating is extra protected by a glass fibre reinforced polymer (GFRP) jacket, with a total diameter of 1 mm to allow embedment of the sensor in harsh environments. A high-resolution FBG interrogator was applied for readouts of wavelengths around 1500 nm.

The optical fibre was equipped with five FBG sensors, which were installed with a base length of 0.8 m or 0.55 m for strain monitoring. At one end of the wall, the optical fibre was bent to enable coverage of two horizontal joints with just one fibre and to increase the robustness of the monitoring system in case of fibre rupture, as the optical fibre can be interrogated from both ends. After installation, only the ends of the optical fibre (pigtails) remained visible as a connection point towards the laser and acquisition system, see Figure 1.

The optical fibre was integrated in the mortar joint of an existing masonry wall specimen (aged over 3 years) during a re-pointing process, carried out one month prior to testing of the wall. Replacement of the pointing mortar is a typical repair intervention for historical masonry [14]. The

installation procedure of the optical fibre sensor was chosen, based on the results of a preliminary test program, which indicated a very low and unreliable adhesion between fibre and mortar. It was therefore opted to fix the optical fibre to small anchors with a depth of 10 cm which were installed on predefined locations in the mortar joints, see Figure 2. The installation process of the optical fibre thus included following subsequent steps: removal of the pointing mortar in two horizontal joints; installation of anchors in drilled holes having 0.8 or 0.55 m between two anchors; fixation of the optical fibre on the anchors with adhesive; repointing of the joint with similar mortar as applied for the original joint; hardening of the fresh mortar joint during 30 days before testing.

Since repointing of joints is a common restoration procedure for historical masonry, this procedure could be applied for integration of the fibre optic sensors on-site, provided that sensor locations are well documented and non-corrosive anchors are applied.

Figure 1: Ends of the optical fibre (pig tails) at the entrance point in the mortar joint

Figure 2: Anchor point and optical fibre in the mortar joint before repointing

2.2 Stereo-vision digital image correlation without speckle pattern

As an optical full-field measurement method, digital image correlation (DIC) has proven to be an ideal tool for a wide range of applications, including the identification of the mechanical material behaviour through inverse modelling, structural health monitoring and the study of the deformation characteristics of a wide range of materials. The basic principle behind the technique is to calculate the displacements on the surface of an object by taking images of a black and white speckle pattern in the undeformed and deformed state. There are three main steps in the DIC method: (1) capturing of images, (2) correlation process and (3) post-processing phase. A detailed analysis of the use of DIC on large-scale masonry samples is given in [15, 16].

A specific problem that arises within the context of the presented study is the speckle pattern typically required to perform DIC measurements. As the use of the DIC technique is here investigated in view of crack monitoring in historic masonry structures, i.e. built heritage, the application of a speckle pattern is to be avoided. Therefore, in this investigation, the texture of the masonry itself is used as a unique pattern for the digital image correlation procedure. This qualifies the DIC measurement as a non-contact method, but has a negative effect on the accuracy of the measurement. The correlation process and the post-processing of the data are done by using MatchID 3D [17]. During the post-processing phase, a commonly adopted method is to calculate the strains by smoothing the displacement data over a certain zone to damp out the effect of noise and local uncertainties. However, in this study, strains were determined directly based on the measured displacements without smoothing of the displacement field to allow for a direct comparison between the data obtained from the DIC measurements and the LVDTs and FBGs.

In the reported study, the area in the middle of the masonry test wall was investigated using a stereovision DIC system, see Figure 3. The zone under investigation, also referred to as the area of interest (AOI), measures approximately 1100 mm by 900 mm (Figure 4). The DIC system consists of two CCD 8-bit cameras with lenses having a focal length equal to 12 mm mounted on a tripod. The cameras are located at a perpendicular distance of approximately 2.2 m from the test specimen. The image acquisition rate of each camera is equal to 2 Hz with an exposure time of 20 ms. All images of the two cameras are transferred to a desktop computer and synchronized with the analogue data (applied force and stroke) of the hydraulic press.

In this contribution, a subset-based method is applied to correlate two images. This method considers a pixel and its neighbourhood in the undeformed image and searches the same subset in the deformed image at a given time step by adopting a maximization routine for a similarity function. The formalism is clearly explained in [17]. In this study, maximization of the similarity function is obtained by adopting the zero-normalized sum of squared differences (ZNSSD) routine. The size of the subset can be chosen as desired prior to the evaluation. The dimensions of each subset were 31 by 31 pixels.

Figure 3: setup of two camera's for DIC measurements

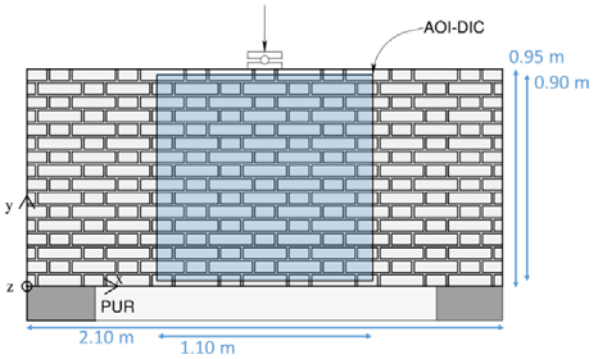

Figure 4: Area of interest of Digital Image correlation (AOI-DIC), in the middle of the wall

2.3 Optical fibre sensors for acoustic emission sensing

The acoustic emission technique is a non-destructive fracture monitoring technique that allows the detection of a crack propagating within a material by detecting and analysing the high-frequency elastic waves produced by the fracture process itself [12]. Analysis of the received waveforms reveals the location and severity of the cracks while individual fracture modes emit signals with different characteristics, enabling the assessment of the dominant fracture mechanism [18-22]. When analysing the AE results, a parameter-based approach applies basic signal characteristics (such as number of AE hits, energy content or amplitude) to deduce information on the fracture process. A waveform-based analysis, which requires high sampling rates and the use of broadband AE sensors, takes into account the complete waveform allowing characterization of the fracture mode [23, 24].

In-situ detection and characterization of acoustic emissions in masonry is complex due to the relatively large dimensions of the structural elements and the anisotropy of the material with respect to wave propagation [25]. This causes excessive wave attenuation and dispersion of the AE signals, while the heterogeneity of masonry leads to further uncertainties in the localization of AE sources and interpretation of the results. Therefore, acoustic emission testing in masonry is

generally performed with resonance-type AE sensors, and parameter-based signal analysis. In literature, the acoustic emission event rate has been correlated to the remaining life of masonry columns under creep or fatigue loading [26, 27] and the rate of crack growth in existing masonry structures [28, 29]. Even if only intensity-based AE-analysis is attempted, the high wave attenuation of masonry poses a serious problem during many in-situ applications.

In this paper, a parameter-based approach is applied and homogeneous wave propagation is assumed to study fracture growth in a full-scale masonry wall subjected to cyclic three-point bending. Standard piezoelectric AE sensors are applied, as well as an optical fibre sensor for AE monitoring. The latter was integrated in the masonry's bed joint in an attempt to cover a larger area with just one AE sensor, addressing the high wave attenuation in masonry.

A brief description of the working principle of the fibre optic sensor for acoustic emission monitoring (AE-FOS) is given here, more information can be found in [11]. The AE-FOS setup works according to the principle of light intensity variations. When damage is initiated, the released elastic energy, in the form of acoustic emissions, perturbs the light in the sensing fibre. In an ideal single mode optical fibre, two polarized optical waves can propagate at the same velocity. External influences, such as ultrasonic waves, introduce birefringence leading to optical anisotropy. Consequently, the two polarized optical waves encounter different refractive indices and propagate at different velocities, causing a phase shift. This birefringence thus causes variations in the polarization of the light at the output of the fibre. In addition to birefringence, the optical fibre also shows a degree of polarization dependent loss, which causes an additional intensity loss of a specific polarization state upon interaction with an acoustic wave. The polarizer at the fibre output isolates a particular polarization state. Not the change in polarization itself, but the change in the light intensity, which varies due to the birefringence, is monitored. Small perturbations of the light intensity indicate the interaction of AE waves with the light that propagates in the fibre optic sensor. The output of the polarizer is led to a photodetector, amplified, filtered and digitized. A disadvantage of the line-integrating technique with a single FOS is that the location of the AE source along the fibre length cannot be determined. This also means that two AE events, occurring within an extremely short time interval (dependent on the sampling rate), cannot be distinguished with the AE-FOS setup.

3 EXPERIMENTAL TEST PROGRAM

3.1 Materials and test setup

The tests are performed on a Flemish bond masonry wall with dimensions 960 x 2100 x 188 mm^3, built up with 16 courses. The wall is made of solid clay bricks with dimensions 188 x 48 x 88 mm^3 and 12 mm thick mortar layers, prepared with fine river sand (0/2 mm, 68 mass%), Portland cement CEM I 42.5 (5.6 mass%), hydraulic lime (11.4 mass%) and water (15 mass%). Standard material testing indicated an average compressive strength of 10 MPa and 3.75 MPa for the bricks and mortar, respectively.

The test wall is subjected to a three-point bending test, as schematically shown in Figure 5. The masonry wall is supported on two concrete blocks, and the area between the support points is filled with polyurethane plates to support the specimen's weight and to avoid collapse of the test specimen after failure had occurred. The experiment is carried out in load control using a hydraulic press. The force of the hydraulic press is applied as a point load at the middle of the top of the wall by means of two steel bearing plates connected with a steel cylinder. To avoid stress concentrations, a layer of gypsum is placed between the masonry test wall and the steel bearing plates. Three cyclic

compression tests were performed on the test wall. During each test, a preload P_0 = 1 KN was applied after which the load was increased at a given load rate $\dot{P}$ until a load value $n \cdot \Delta P$, with n equal to the number of the cycle. The load was decreased after each cycle until the selected preload was again obtained. In between the three tests, the specimen is fully unloaded. An overview of the load parameters is given in Table 1. During the third compression test, failure of the masonry wall occurred. The failure load is indicated in bold.

Table 2 indicates the specifications of the applied sensors. The placement of the sensors on the masonry wall is schematically presented in Figure 5. Optical fibres (FBG sensors and AE-FOS) were integrated in the bed joints, thus not visible on the wall's outer surface.

Table 1: Loading scheme parameters

	$\dot{P}$ [kN/s]	*n total* [-]	ΔP [kN]	P_{max} [kN]
test 1	0.033	5	2.0	10.0
test 2	0.083	10	5.0	50.0
test 3	0.333	4	20.0	**76.4**

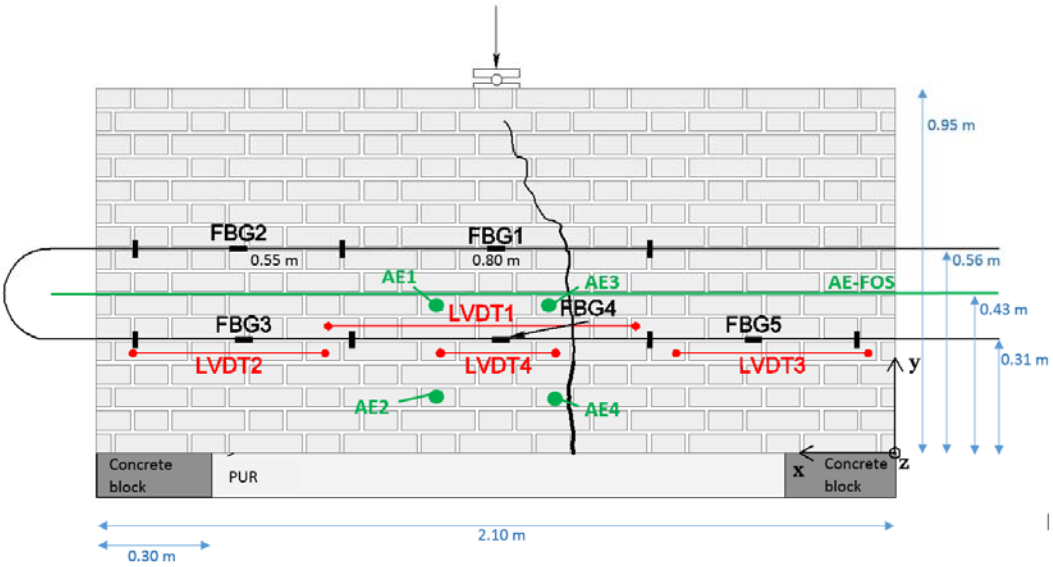

Figure 5: Test setup of three-point bending test on masonry wall, with indication of the positions of sensors and the major crack that occurred at the end of test 3.

Table 2: Overview of applied sensors, with reference to Figure 5.

abbreviation	Sensor type	# sensors	specifications	remarks
AE(-PZT)	PZT-type AE sensor	4	VS150-M, 100-450 KHz, resonance at 150 KHz	connected on outer surface with hot melt glue
AE-FOS	optical fibre	1 (1 optical fibre)	single mode optical fibre in GFRP tape, width 12 mm, thickness 0.3 mm	integrated in mortar joint during bricklaying
FBG(-FOS)	optical fibre with fibre Bragg grating sensors	5 (5 FBG on 1 optical fibre)	SMW-01 optical fibre, with GFRP jacket (1 mm diameter). Wavelengths around 1500 nm.	integrated in the mortar joint during re-pointing, connected to anchor points (0.55 or 0.80m in between)
LVDT	strain sensor: linear variable differential transducer	4	range of 10 mm	mechanically fixed to the masonry, base lengths of 0.30-0.50-0.80 m
DIC	digital image correlation with two camera's	/	two CCD 8-bit cameras at 2.2 m from the wall, AOI is 1100 mm by 900 mm	Measurement taken on opposite side of the wall from which other sensors are installed

3.2 Observed crack growth

During test 1, no damage was detected. The only sound results obtained from test 1 were elastic strains monitored by the FBGs and LVDTs in the order of 5 µm/m or 0.005 ‰, which is well below the ultimate tensile strain of the masonry. Therefore, the results of test 1 are not discussed further. In test 2, no visual damage was observed. During test 3, small vertical cracks were visually observed in the mortar joint and lower bricks from a load of 60 kN (cycle 3). In the next load cycle, these cracks coalesced into a large macro crack (see Figures 5 and 6) after which the test was stopped. Damage was observed at a much earlier stage by the AE and strain sensors, as discussed below. The major crack did not appear in the central (symmetric) position in the wall, indicating that asymmetry had been present in the material properties, geometry and/or boundary conditions.

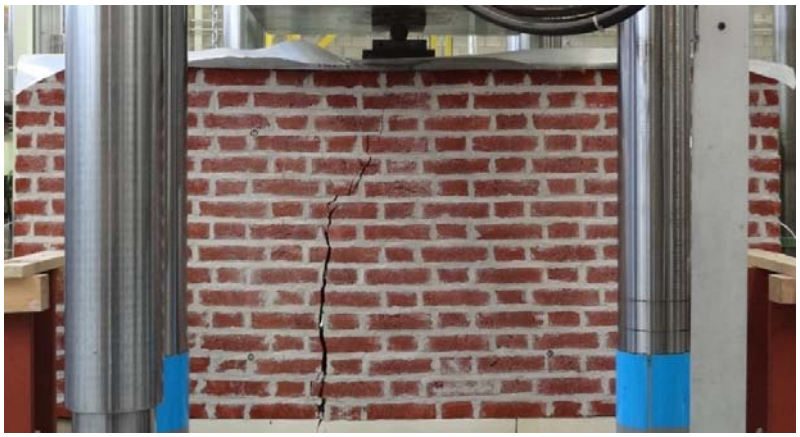

Figure 6: Macro crack in the masonry wall at the end of test 3.

4 RESULTS AND DISCUSSION

4.1 Results: Strains and displacements

Results obtained during test 2 and 3 are presented in Figure 7. The strain data, obtained from the FBG interrogation during the tests, are converted into deformations by multiplication with the appropriate base length, 0.8 m or 0.55 m respectively. This implies the assumption that there is no adhesion between the optical fibre and the mortar and that the strains within the FBGs are similar to strains at other locations between two anchor points. Such is only correct in the absence of stress concentrations at the beginning of the test and towards the end of the test when larger deformations occur and the adhesion between mortar and optical fibre is completely lost. For reference, the results of the LVDTs are also presented. The observed noise level, which is related to the accuracy of the measurement, was around 2.0 µm for the LVDTs and 0.8 µm for the FBGs. Both techniques were able to capture the elastic deformations and the onset of cracking. In comparison, the FBGs demonstrated better accuracy and robustness. In each test, one out of four LVDTs (LVDT1) did not work properly due to friction between the moving and fixed parts. All FBGs performed well during the three tests and reliable deformation data were obtained, which followed the force application scheme (see Figure 7).

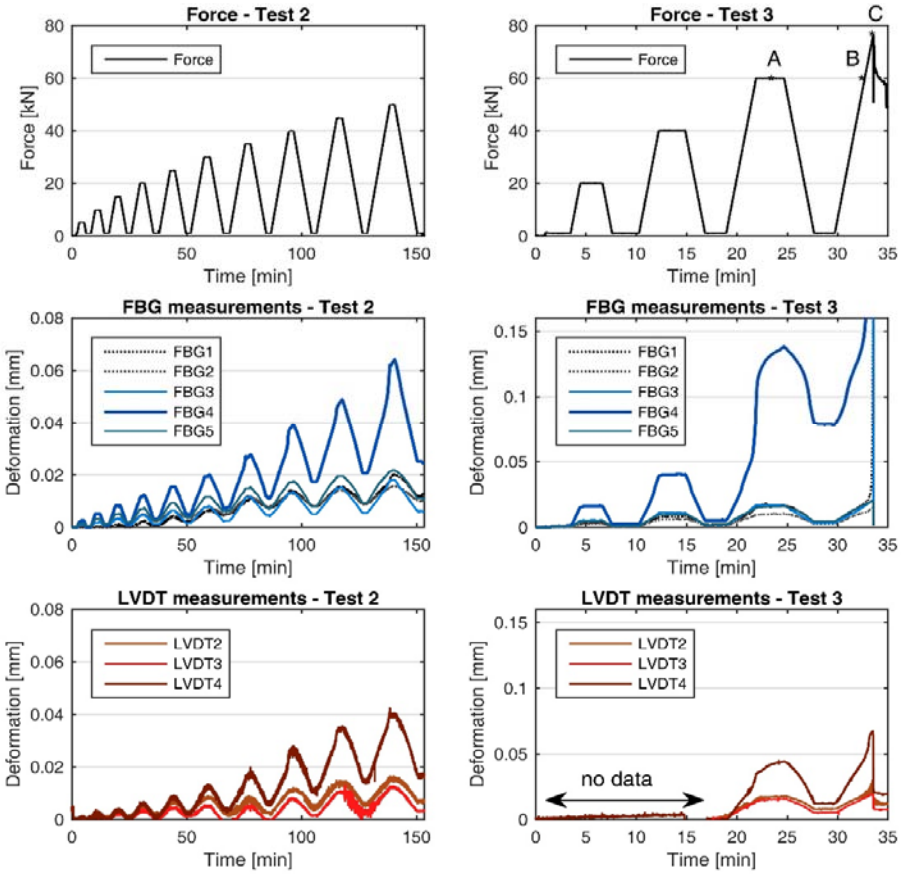

Figure 7: Applied force (top), deformations measured with FBGs (mid) and with LVDTs (bottom) during cyclic three-point bending test 2 (left) and test 3 (right). Results of LVDT 1 are not show. See Figure 5 for sensor setup and macro crack location.

With the digital image correlation technique, full field 2D deformation data are obtained. Figure 8 (a) presents the measured vertical displacement field u_y as a function of the surface coordinates at 60 kN during test 3 (point A in Figure 7) whereas Figure 8 (b) shows the same vertical displacement field near failure (point B in Figure 7). Finally, Figure 8 (c) shows the horizontal displacement field u_x at the experimentally measured failure load. The latter clearly shows the location and shape of the macro crack. It can be seen from Figure 8 (c) that the crack tip acts as a hinge. The left part of the wall rotates clockwise around the crack tip whereas the right part undergoes a rotation counter-clockwise. The displacements occurring at lower load levels were found to be too small to be accurately measured by the stereo-vision digital image correlation technique from a distance of 2.2 m without the use of a speckle pattern.

The resolution of the digital image correlation, i.e. the smallest signal above the noise level, was quantified by correlating two different images in undeformed state and assessing the predicted displacements. The noise on the displacement data can be considered normally distributed and can therefore be best expressed by the standard deviation of the considered displacement component. For this setup, the standard deviation of the horizontal and vertical displacement components u_x and u_y were found to be equal to 0.065 mm respectively 0.058 mm. As can be observed in Figure 7, displacements above this level are only recorded from the second to last loading step in test 3, at the moment the crack was observed. The standard deviation of the out-of-plane displacement u_z is an order of magnitude higher (equal to 0.449 mm). However, this displacement component is also less important for the reported experiments since primarily in-plane displacements and deformations occur.

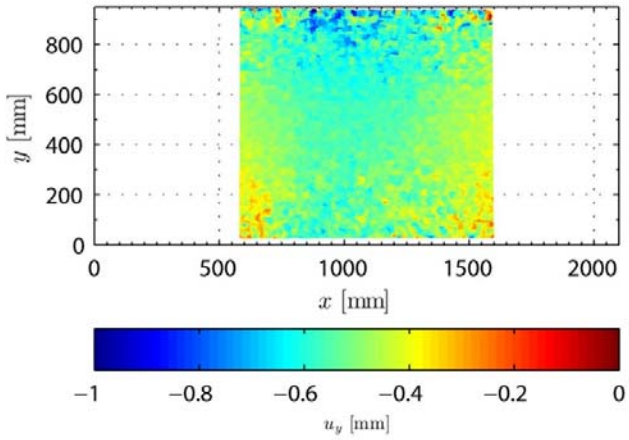

a) Vertical displacement u_y, P = 60 kN (point A in Figure 7)

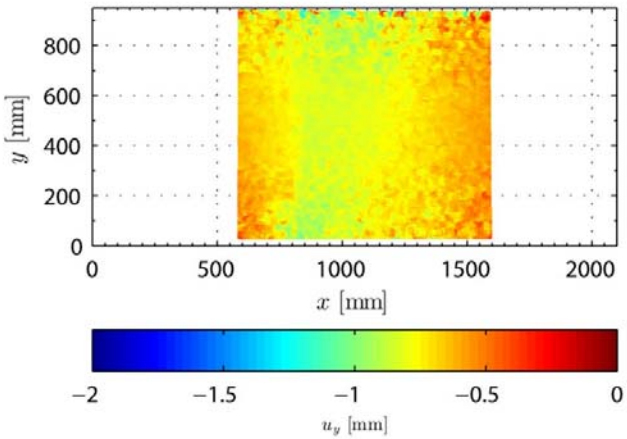

b) Vertical displacement u_y, (point B in Figure 7)

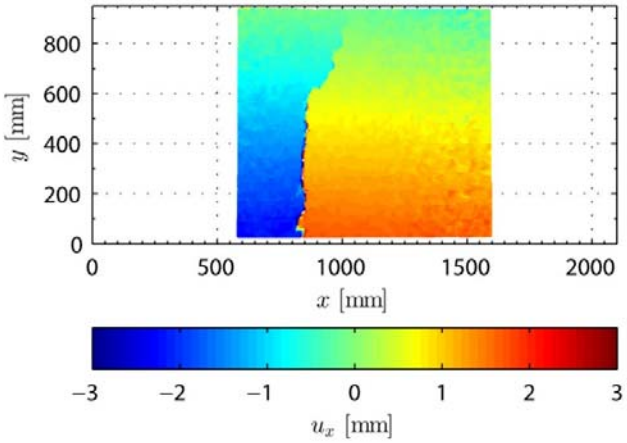

c) Horizontal displacement u_x, P = 76.4 kN (point C in Figure 7)

Figure 8: Experimental displacement field from DIC measurements as a function of the surface coordinates at various load levels

4.2 Results: Acoustic emission data

Four PZT-type acoustic emission sensors were positioned in the lower middle area of the wall, at a distance of 24 cm (vertically) and 29 cm (horizontally), see Figure 5. A threshold of 34 dB was applied for AE event detection. As the maximum source-sensor distance observed in the masonry wall was limited to an average of 30 cm (depending also on the number of joint crossings), and the crack unexpectedly occurred outside of the rectangular area defined by the AE sensors' position, no accurate source location data could be obtained. Therefore, AE data in Figure 9 are not shown as located events, but as AE energy monitored by each of the four individual AE sensors. The energy unit is defined as 1eu = 1E-14V²s. In addition, crack localisation was merely based on the location of the nearest AE-PZT sensor (firstly) detecting the AE event.

The optical fibre for acoustic emission monitoring (AE-FOS) was positioned at a height of 0.43 m from the bottom of the wall, in between the two lines of FBG sensors and just above the

piezoelectric AE sensors. For the masonry wall, the detection range of the AE-FOS was found to be limited to 2 cm on each side along the optical fibre. In concrete, acoustic emissions could be detected up to a range of 5-10 cm in a previous test program [11].

AE-PZT sensor 2 and 4, both located near the tension zone at the bottom of the wall clearly detect a higher AE energy level from the start of test 2 (Figure 9). Halfway through test 2, when the micro cracking localizes near sensor 4, the AE activity detected by sensor 2 falls back. In the last load step of test 2, it is likely that micro cracking has reached AE sensor 3 as an increase in AE energy is detected. However, this is not confirmed by the measurements of the AE-FOS. In test 3, it is clear that the asymmetric macro crack is located near AE sensor 4, as this sensor detects the highest AE energy during loading, but also during unloading, which indicates friction in the existing cracks. At the final cycle, AE sensor 3 detects the highest amount of AE events (max. values are not shown). At this point, the AE-FOS detects a major increase in AE activity, just before rupture of the fibre (Figure 10). The limited (vertical) range of the AE-FOS in masonry hindered an accurate detection of AE activity by this sensor at an earlier stage during the test.

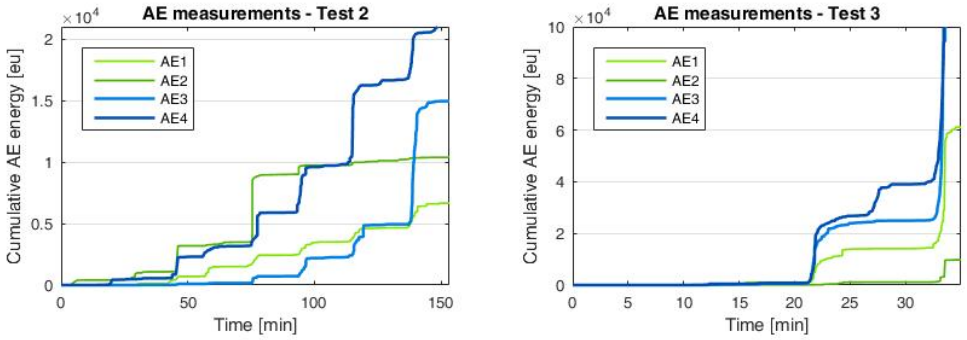

Figure 9: Cumulative AE energy measured by each of the four AE-PZT sensors, test 2 (left) and test 3 (right)

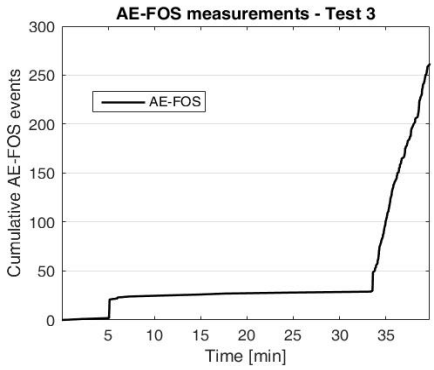

Figure 10: Cumulative number of AE events detected by the optical fibre (AE-FOS) during test 3

During cyclic testing, the Kaiser effect as well as Felicity effect were observed [12]. Both effects are presented in Table 3, based on the results of the AE-PZT sensors. The calculated values in Table 3 are the ratios between the load level at which first AE activity is observed during a load cycle, divided by the maximum load obtained in the previous load cycle. This is also called LOAD ratio (ratio of Load at

the Onset of AE Activity to previous load, [12]). Here, the start of AE activity in a load cycle is arbitrarily defined as the occurrence of at least 3 AE events in a time interval of 10 seconds. The value >1 indicates that too little AE activity was registered by a sensor to determine the start of AE activity in that cycle. The Kaiser Effect concerns the 'memory' of the material for previously obtained maximum load levels and indicates that AE activity only starts when a previous maximum load is exceeded again. This is evidenced in the first test cycles by values higher than or around a ratio of 1. At higher load levels, acoustic emissions are recorded even if the previously applied maximum load level is not yet exceeded, indicated by values smaller than 1. This is called Felicity effect and is evidence of substantial structural defects.

Lower values in table 3 towards the end of the test are thus evidencing growth and coalescence of micro cracking in the masonry. This effect is clearly observed towards the end of test 2 for AE sensor 4, which is the sensor nearest to the final macro crack. At this point, no visual cracking had yet been observed. In table 3, no values are available for the first row, as the load in this cycle remained lower than the maximum load obtained in test 1. A slight discontinuity is also observed between the last cycle of test 2 and the first cycle of test 3 in which the previous maximum load is exceeded (being cycle 3, at 60 kN). The overnight unloading of the specimen and temperature fluctuations might have caused partial crack closure and microstructural shifts which influenced the AE activity in such a way that AE activity in test 3 was observed at slightly lower load levels than expected. On the other hand, this step also coincides with the visual observation of the macro crack in the masonry. It can thus be concluded that the evolution of the Felicity effect was very consistent with the observed cracking.

Table 3. Ratio between load at first AE activity in a cycle and maximum load during previous cycle. (sensor 4 = crack location). Severe damage is assumed for values below 0.90.

	cycle	sensor 1	sensor 2	sensor 3	sensor 4
test 2	1	/	/	/	/
	2	› 1	› 1	› 1	› 1
	3	› 1	› 1	› 1	1.50
	4	1.14	1.27	› 1	1.34
	5	1.07	› 1	› 1	1.05
	6	1.08	1.10	1.20	1.04
	7	1.10	1.15	1.07	1.05
	8	1.05	1.09	1.09	0.87
	9	0.91	1.09	1.09	0.86
	10	0.95	0.90	0.99	0.86
test 3	*3*	*0.87*	*1.20*	*0.87*	*0.86*
	4	*0.67*	*0.99*	*0.58*	*0.51*

4.3 Effect of temperature fluctuations

The influence of temperature fluctuation on the sensor output has been quantified in the 16-hour time interval between test 2 and 3, in order to assess its importance for future on-site applications.

Within this time period, temperature fluctuations, strain data (FBGs) and acoustic emissions (AE-PZT) were continuously monitored. Temperature changes were induced in an uncontrolled manner by switching off the heating system in the lab overnight (slow temperature decrease) and opening the lab gates the next morning (fast temperature decrease).

Temperature fluctuations cause a dual effect on the strains measured with the Fibre Bragg Grating sensors. Firstly, the glass fibre elongates according to its coefficient of thermal expansion. Since the optical fibre is integrated in the masonry, the thermal expansion coefficient of clay brick masonry (4-5 10^{-6} K^{-1}) can be assumed for this part. Secondly, the temperature change causes a shift in the refraction index, resulting in a shift in reflected wavelength and thus an erroneous strain. The temperature sensitivity of the applied FBG sensors equals 6.5 10^{-6} K^{-1} in the range between 0-70°C. A relation between wavelength, mechanical strains and temperature fluctuations can be expressed as:

$$\frac{\Delta\lambda}{\lambda_0} = k \cdot \left(\varepsilon_m + \alpha_{sp} \cdot \Delta T\right) + \alpha_\delta \cdot \Delta T \qquad (1)$$

With:

$\Delta\lambda =$ the shift in wavelength [nm]
$\lambda_0 =$ the initial wavelength [nm]
$k =$ a correlation factor, relating the wavelength shift and strain [7.77 10^{-7} $\mu\varepsilon^{-1}$]
$\varepsilon_m =$ the mechanical strain [-]
$\alpha_{sp} =$ the thermal expansion coefficient of the optical fibre, or of the structure to which the fibre is connected [K^{-1}]
$\alpha_\delta =$ a correction factor to take into account the shift in refraction index upon temperature fluctuations [K^{-1}]
$\Delta T =$ the temperature fluctuation [°C] or [K]

The values that were monitored in the 16-hour time interval between test 2 and 3 are indicated in Figure 11. During the overnight slow temperature decrease (period A), the FBG strain sensors measure a negative strain (contraction), and the AE sensors measure a low number of AE events with a diminishing amount of detected events over time. This measurement was started at the end of test 2, so crack closure might have influenced the detected AE events at the start of the measurement. A positive deformation (expansion) is detected by the FBGs upon temperature increase, while very few AE events are detected during time period B. The opening of the lab gates (period C) does lead to a negative strain measured by the FBGs and a slightly increased detection of AE events. The overall amount of events detected by the AE sensors is negligible and can partly be ascribed to unfiltered background noise and friction in existing cracks.

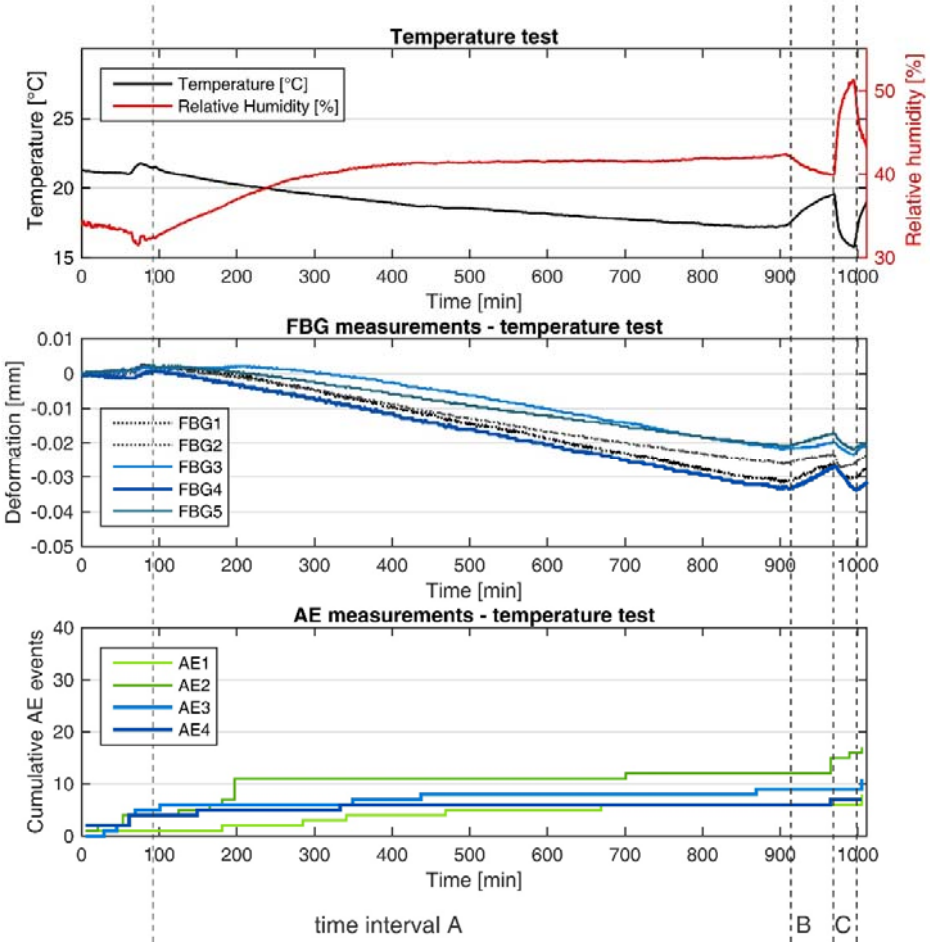

Figure 11: Strain and AE data obtained during temperature fluctuation test.

Table 4 presents the overall thermal coefficients for all FBG sensors, averaged within each time period. This coefficient is related to the slope of the displacement graphs in Figure 11, and equals the following equation:

$$\alpha_{\Delta T} = \frac{\Delta x}{\Delta T} = \alpha_{sp} + \frac{\alpha_{\delta}}{k} \qquad (2)$$

as derived from equation (1). It can be observed from equation (2) that the correction factor for the refraction index has a much larger effect on the strain shift than the thermal expansion coefficient of the masonry, as the correlation factor, *k*, is very small.

For time period A, the calculated overall thermal coefficients indicated in Table 4 are slightly higher than the theoretical coefficient, $\alpha_{\Delta T} = 8.37\ \mu\varepsilon \cdot K^{-1}$, calculated according to the right term in equation (2). This might be an indication of crack closure during the temperature test, as it results in negative strains that are higher in absolute value than the theoretical thermal effects.

As expected, too low overall thermal coefficients are calculated for time periods B and C. This indicates that the masonry lags behind with respect to the measured air temperature and humidity. These latter time periods are too short to allow the masonry to reach thermal equilibrium with the

surrounding air, and thermal expansion/contraction of the masonry to take place. The non-linear response of the masonry-sensor system with respect to temperature fluctuations indicates the necessity to apply non-stressed, reference sensors during on-site monitoring.

Table 4. Calculated overall thermal coefficients for all FBG sensors, averaged within each time period (time intervals indicated in Figure 11).

		time period A	**time period B**	**time period C**
ΔT [°C]		4.26	-1.87	3.36
$\alpha_{\Delta T}$ [με·K^{-1}]	FBG 1	9.27	2.25	1.25
	FBG 2	11.58	2.24	1.74
	FBG 3	10.55	0.89	1.49
	FBG 4	9.92	3.11	1.48
	FBG 5	9.30	2.65	1.97
av. $\alpha_{\Delta T}$ [με·K^{-1}]		**10.12**	**2.23**	**1.59**

4.4 Discussion and remarks

A comparison between the experimentally observed crack growth and the results of the acoustic emission and strain monitoring shows good consistency in the data, with the PZT-type AE sensors and the FBG-type strain sensors giving most reliable and useful data sets for crack monitoring in the masonry wall.

After occurrence of the large macro crack during test 3, the two types of optical fibres that were integrated in the bed joints showed different response: The optical fibre that was equipped with fibre Bragg grating sensors (FBG-FOS) had slipped from the mortar joints and remained operational. This optical fibre was only connected at specific anchor points, which were placed at a distance of 0.55 or 0.80 m within the masonry. The maximum recorded strain of 1% (averaged over a base length of 0.8 m) did not exceed the optical fibre's maximum tensile strain of 2.5 %. Therefore, FBG measurements could continue after occurrence of a major crack. A slight crack closure was measured during unloading and all FBGs still recorded the two force cycles up to 10 kN which were imposed on the wall after unloading (not shown on the graphs). The AE-FOS on the other hand had ruptured. This optical fibre requires good contact with the masonry along its length to transfer high frequency, low amplitude waveforms. Therefore, this fibre was designed not to slip with respect to the mortar joint, and thus could not accommodate the localized high strains at the location of the macro crack at the end of test 3.

During the temperature test, it was observed that temperature fluctuations cause a dual effect on strains measured with Fibre Bragg Grating sensors. Both temperature effects can be dealt with during on-site measurements by placing an additional FBG sensor on a non-stressed part of the structure, and subtracting the measured value (which includes the thermal expansion of the masonry and the temperature sensitivity of the FBG sensor) from the actual monitoring data. If there is no availability of a non-stressed part of the structure, which follows the same temperature loading as the monitored part, a sensor should be placed which is not connected to the structure. In this case, the expansion of the masonry is additionally to be compensated in the monitoring data.

5 CONCLUSIONS

Several novel types of strain and acoustic emission sensors were investigated for crack monitoring in masonry structures. A full-size masonry wall was constructed and subjected to cyclic three-point bending tests with increasing intensity. Based on the experimental results, it was observed that for crack measurements in large (historical) masonry elements, a combination of resonance-type AE sensors and optical fibres equipped with FBGs provides optimal crack detection. The optical fibre with semi-distributed FBGs can cover larger distances and performs excellently for crack width quantification, provided that temperature compensation is foreseen. When a crack tip is identified, the AE sensors positioned within a region of several decimetres around the crack tip are able to register the moment of occurrence of crack growth and friction-related AE events, and to detect unstable crack growth well in advance.

This study is part of a project that aims at the application of novel techniques for on-site damage monitoring and risk assessment in historical masonry structures that are subjected to settlement-induced damage. Therefore, future objectives are to up-scale the developed systems and to link on-site monitoring data with differential settlement maps obtained through high-resolution PS-InSAR measurements, allowing risk assessment of historical masonry structures with respect to ground settlements.

ACKNOWLEDGMENTS

This work is performed within the framework of the GEPATAR project (“GEotechnical and Patrimonial Archives Toolbox for ARchitectural conservation in Belgium” BR/132/A6/GEPATAR), which is financially supported by BRAIN-be, Belspo.

REFERENCES

[1] Verstrynge E., Van Gemert D. Multi-scale approaches for the assessment of time-dependent mechanical damage in masonry. in Structural Analysis of Historical Constructions - SAHC 2016. Leuven, Belgium: CRC/Balkema. 2016, p. 54-64.

[2] Binda L., Saisi A. Application of NDT's to the diagnosis of historic structures, in 7th International symposium on non destructive testing in civil engineering, Abraham O., Derobert X., Editors: Nantes. 2009. p. 43-69.

[3] Ramos L.F., De Roeck G., Lourenço P.B., Costa A.C. Vibration Based Damage Identification of Masonry Structures, in Structural Analysis of Historical Constructions, Lourenço P.B., et al., Editors: New Delhi. 2006. p. 641-649.

[4] Gentile C., Saisi A. Ambient vibration testing of historic masonry towers for structural identification and damage assessment. Construction and Building Materials 2007; 21(6):1311-1321.

[5] Kapogianni E., Kalogeras I., Psarropoulos P.N., Giokaris S., Sakellariou M.G. Structural health monitoring of the Athenian Acropolis' Walls via optical fibre sensors, accelerographs and numerical simulation, in Structural Analysis of Historical Constructions - Anamnesis, diagnosis, therapy, controls, Van Balen K., Verstrynge E., Editors. CRC/Balkema: Leuven. 2016. p. 701-708.

[6] Ceriotti M., Mottola L., Picco G.P., Murphy A.L., Guna S., Corra M., et al. Monitoring heritage buildings with wireless sensor networks: The Torre Aquila deployment, in IPSN. ACM: San Francisco. 2009. p. 277-288.
[7] Clarke J.A., Laefer D.F. Systematic Approach for Large-Scale, Rapid, Dilapidation Surveys of Historic Masonry Buildings. International Journal of Architectural Heritage 2014; 8(2):290-310.
[8] Tapete D., Fanti R., Cecchi R., Petrangeli P., Casagli N. Satellite radar interferometry for monitoring and early-stage warning of structural instability in archaeological sites. Journal of Geophysics and Engineering 2012; 9(4):S10-S25.
[9] Bejarano Urrego L., Verstrynge E., Van Balen K., Wuyts V., Declercq P. Settlement-induced damage monitoring of a historical building located in a coal mining area using PS-InSAR, in 6th Workshop on Civil Structural Health Monitoring, Taylor S., Editor: Belfast. 2016. p. art.nr. S-3 4.
[10] Othonos A., Kalli K. Fiber Bragg Gratings: Fundamentals and Applications in Telecommunications and Sensing. Norwood, MA, USA: Artec House. 1999.
[11] Verstrynge E., Pfeiffer H., Wevers M. A novel technique for acoustic emission monitoring in civil structures with global fiber optic sensors. Smart Materials and Structures 2014; 23(6):065022.
[12] Grosse C.U., Ohtsu M., eds. Acoustic emission testing - basics for research - applications in civil engineering. Springer. (2008).
[13] Luyckx G., Voet E., Lammens N., Degrieck J. Strain Measurements of Composite Laminates with Embedded Fibre Bragg Gratings: Criticism and Opportunities for Research. Sensors (Basel, Switzerland) 2011; 11(1):384-408.
[14] Van Roy N., Van Balen K., Verstrynge E., Naldini S. The stratified significance of a historic façade as a basis for a more durable conservation approach. Restoration of Buildings and Monuments 2015; 21(4-6):137-148.
[15] Mojsilovic N., Salamanpour A.H. Masonry walls subjected to in-plane cyclic loading: application of digital image correlation for deformation field measurement. Int. J. Masonry Research and Innovation 2016; 1(2):165-187.
[16] Ghorbani R., Matta F., Sutton M.A. Full-Field Deformation Measurement and Crack Mapping on Confined Masonry Walls Using Digital Image Correlation. Experimental Mechanics 2015; 55(1):227-243.
[17] Lava P., Cooreman S., Coppieters S., De Strycker M., Debruyne D. Assessment of measuring errors in dic using deformation fields generated by plastic fea. Optics and Lasers in Engineering 2009; 47(7-8):747-753.
[18] Ohno K., Ohtsu M. Crack classification in concrete based on acoustic emission. Construction and Building Materials 2010; 24(12):2339-2346.
[19] Shiotani T. Evaluation of long-term stability for rock slope by means of acoustic emission technique. Ndt & E International 2006; 39(3):217-228.
[20] McLaskey G.C., Glaser S.D., Grosse C.U. Beamforming array techniques for acoustic emission monitoring of large concrete structures. Journal of Sound and Vibration 2010; 329(12):2384-2394.
[21] Aggelis D.G., Soulioti D.V., Sapouridis N., Barkoula N.M., Paipetis A.S., Matikas I.E. Acoustic emission characterization of the fracture process in fibre reinforced concrete. Construction and Building Materials 2011; 25(11):4126-4131.
[22] Verstrynge E., Wevers M., Ghiassi B., Lourenço P.B. Debonding damage analysis in composite-masonry strengthening systems with polymer- and mortar-based matrix by means of the acoustic emission technique. Smart Materials and Structures 2016; 25(1):015009.
[23] Grosse C.U., Finck F. Quantitative evaluation of fracture processes in concrete using signal-based acoustic emission techniques. Cement and Concrete Composites 2006; 28(4):330-336.

[24] Linzer L., Mhamdi L., Schumacher T. Application of a moment tensor inversion code developed for mining-induced seismicity to fracture monitoring of civil engineering materials. Journal of Applied Geophysics 2015; 112:256-267.
[25] Livitsanos G., Shetty N., Verstrynge E., Wevers M., Van Hemelrijck D., aggelis D.G. Characterization of Fracture Mode in Masonry by Acoustic Emission, in 32nd European Conference on Acoustic Emission Testing, Mazal P., Pazdera L., Editors: Prague, Czech Republic. 2016. p. 287-295.
[26] Verstrynge E., Schueremans L., Van Gemert D., Wevers M. Monitoring and predicting masonry's creep failure with the acoustic emission technique. NDT & E International 2009; 42(6):518-523.
[27] Tomor A.K., Verstrynge E. A joint fatigue–creep deterioration model for masonry with acoustic emission based damage assessment. Construction and Building Materials 2013; 43:575-588.
[28] Carpinteri A., Lacidogna G. Damage evaluation of three masonry towers by acoustic emission. Engineering Structures 2007; 29(7):1569-1579.
[29] Tomor A.K., Melbourne C. Condition monitoring of masonry arch bridges using acoustic emission techniques. Structural Engineering International 2007; (2):188-192.